Materials Advances

Accepted Manuscript

This article can be cited before page numbers have been issued, to do this please use: R. Anwar, C. Ton-That and Md. A. Rahman, *Mater. Adv.*, 2026, DOI: 10.1039/D5MA01263E.

ROYAL SOCIETY OF CHEMISTRY

rsc.li/materials-advances

DOI: 10.1039/D5MA01263E

Modulating the visible emission and whispering gallery mode lasing through the self-induced defects in a Ga-doped ZnO tapered microcavity

Rubia Anwar[1], Cuong Ton-That[2], and M. Azizar Rahman[1,*]

[1]*Department of Physics, Bangladesh University of Engineering and Technology, Old Academic Building, Dhaka-1000, Bangladesh*

[2]*School of Mathematical and Physical Sciences, University of Technology Sydney, Ultimo, NSW 2007, Australia*

[*]Corresponding author. Email: azizar@phy.buet.ac.bd

Abstract

Achieving low-order visible whispering gallery mode (WGM) lasing in monolithic semiconductor microcavities is typically hindered by poorly controlled defect emission and limited dispersion control. We address this by co-designing the gain spectrum and cavity geometry in single, tapered Ga-doped ZnO (GZO) hexagonal microrods grown by vapor-phase deposition. Ga incorporation forms Ga–native-acceptor complexes that red-shift and broaden the deep-level band, creating a tunable 500–600 nm gain window. Concurrently, the built-in diameter gradient (0.73–2.5 μm) deterministically selects WGM order along the same resonator, enabling continuous tuning of WGM order from N = 29 to N = 3–5. Plane-wave analysis and finite-element simulations accurately reproduce the measured path lengths, mode numbers, and linewidth evolution. By uniting defect-state engineering with geometry control in a single cavity, without the use of coupled resonators, plasmonics, or heterostructures, this approach enables the delivery of compact, spatially addressable, low-order visible microlasers for integrated photonics.

Keywords: whispering-gallery microlasers; Ga-doped ZnO; tapered microcavities; defect engineering; electron-beam pumping

View Article Online
DOI: 10.1039/D5MA01263E

1 Introduction

Wide-bandgap ZnO (E_g ≈3.3 eV) with a large exciton binding energy and robust transport underpins micro/nanolasers and LEDs, yet compact, low-order visible whispering-gallery-mode (WGM) lasing in a single monolithic cavity remains elusive. Two long-standing bottlenecks are (i) uncontrolled deep-level (green–yellow) emission that governs the available gain spectrum and (ii) insufficient geometric control of cavity dispersion and mode order in stand-alone microresonators. Prior strategies often rely on UV excitonic gain, cryogenic operation, or coupled cavities; these compromise integration and spatial programmability. Here, we address both bottlenecks simultaneously through defect–cavity co-design in single, hexagonal Ga-doped ZnO (GZO) microrods. On the gain side, Ga donors interact with native acceptors (V_{Zn},O_i) to form Ga-acceptor complexes that red-shift and broaden the deep band, yielding a tunable 500–600 nm gain window for visible lasing. On the cavity side, a growth-defined axial diameter gradient **(**~0.73–2.5 μm**)** tailors the local WGM dispersion, enabling the deterministic selection of lower azimuthal orders toward the taper tip and concomitantly larger free-spectral range.

ZnO supports a large family of nano/microstructures, including nanowires, nanorods, and hexagonal microrods, which can be grown more readily than other oxide and nitride-based semiconductors. Among these, hexagonal microrods have the potential for whispering gallery mode (WGM) resonators, in which light-waves can be trapped inside the cavity owing to multiple internal reflections at the six-fold boundaries of the hexagon. These WGM resonators are highly important for understanding the physics of light-matter interaction and are in demand for the application of photonic devices,[1, 2] lasing,[3, 4] biosensing,[5, 6] virus detection,[7] second harmonic light generation,[8] small molecules sensing,[4] optical patterning,[9] and optical modulating.[10, 11] The visible (green to red) WGM lasing in ZnO has been demonstrated in different resonant cavities, including random,[12-14] Fabry-Pérot,[15-17] and WGM[18, 19]

View Article Online
DOI: 10.1039/D5MA01263E

configurations. Among them, the WGM lasing is a promising candidate due to its low lasing threshold and high-quality factor, which are particularly important for practical applications. In hexagonal ZnO, WGM lasing spans a wide range of mode numbers, from low-order (mode number $N < 6$) in the visible,[20] to high-order ($N > 60$), ultraviolet,[21] with reports of WGM polaritons ($N < 10$),[22] and second-harmonic WGMs ($N < 8$). [23] The number of lasing modes is dependent on the size of the cavity and excitation power density.[21, 24] Single-mode ultraviolet WGM lasing has been reported in ZnO nanorods by adjusting the cavity size.[21, 25] However, low-order ($N \leq 5$) WGM lasing in the visible range (500 – 600 nm) from a single monolithic hexagonal ZnO microcavity, with deterministic, size-dependent tuning, has not been demonstrated.

In this work, we demonstrate visible WGM microlasing in single, tapered Ga-doped ZnO hexagonal microrods by co-designing gain and cavity dispersion. Ga incorporation broadens and red-shifts the deep-level emission to provide visible gain, while the growth-defined axial taper controls the local WGM dispersion and selects lower azimuthal orders toward the tip. Under electron-beam excitation, a single microrod supports spatially addressable, low-order visible microlasing along its length without the need for coupled resonators. The WGM lasing behavior is quantitatively interpreted using classical plane-wave analysis and finite-element eigenmode simulations.

2 Experimental methods

2.1 Synthesis of Ga-doped ZnO nanorods

ZnO nanorods were deposited on a Si substrate by the vapor-phase deposition method explained earlier.[26] The wafers were cleaned using isopropanol, acetone, and deionized water, followed by a blow-dry with nitrogen gas. A 5 nm gold layer was deposited on the precleaned substrate. ZnO and graphite powders (in a 1:1 ratio) were thoroughly mixed and loaded into the tube furnace in two separate boats to fabricate ZnO nanowires. ZnO and graphite powders

View Article Online
DOI: 10.1039/D5MA01263E

were mixed using a mortar for several hours until the mixture became visually homogeneous. The argon and oxygen flow rates were 5:25 sccm. To deposit GZO nanorods, Ga_2O_3 powder (Sigma Aldrich, 99.99% pure) was mixed with the source material. For a Ga concentration of 0.13 at%, 0.75 mg Ga_2O_3 and 999.25 mg ZnO, while for a 0.5 at% Ga concentration, 2.87mg Ga_2O_3, and 997.13 mg ZnO were used as source material.

2.2 Synthesis of Ga-doped ZnO microrods

ZnO microrods were grown on Si substrates coated with a thin ZnO buffer layer prepared by spin coating, which acted as a nucleation layer. The coated substrates were positioned above an alumina boat containing a pre-prepared powder mixture of ZnO and Ga_2O_3. At 900 ºC, the alumina boat containing the source material was inserted into the center of the furnace and kept at a fixed temperature of 1100 ºC for 5–10 min, followed by rapid quenching. Zn and Ga vapors formed via carbothermal reduction of ZnO and Ga_2O_3 and subsequently reoxidized in the oxygen flow, driving microrod growth. A detailed description of the growth of taper microrods has been described previously.[27]

2.3 Characterization

Morphological and elemental mapping were performed by a Zeiss Supra 55VP scanning electron microscope (SEM) equipped with an Energy Dispersive X-ray (EDX) spectrometer. Selected-area electron diffraction (SAED) patterns were collected using a FEI Tecnai T20 transmission electron microscope (TEM). Laser ablation (Teledyne Cetac LSX-266) inductively coupled plasma mass spectrometry (Agilent 7500cx）(LA-ICP-MS) was used to control the elemental composition of the pristine and Ga-doped ZnO nanorods. X-ray photoemission spectroscopy (XPS) analyses were conducted at a photon energy of 1486 eV on the Soft X-ray Spectroscopy (SXS) beamline at the Australian Synchrotron. Cathodoluminescence (CL) spectra were collected in spot mode using a FEI Quanta 200 SEM coupled to a high-resolution Hamamatsu spectrometer. The steady-state CL and WGM spectra

View Article Online
DOI: 10.1039/D5MA01263E

were collected using an acceleration voltage of 7 kV, beam current of 4 nA, and an electron-beam spot size of approximately 200 nm. For the excitation-power-dependent lasing measurements, the acceleration voltage was 10 kV, and the beam current was varied to determine the lasing threshold.

3 Results and discussion

3.1 Structure and morphology of Ga-doped ZnO nano- and micro-rods

Fig. 1 (a) shows the SEM of Ga-doped ZnO nanorods grown onto a-plane Si substrate. For length and diameter measurement, the sample was sonicated in acetone and drop-cast on a TEM grid to isolate a single nano/microrod. The diameter of the nanorod varies from 50 to 100 nm, and its length is several μm. Fig. 1 (b) displays the top view of GZO microrods grown by a refined vapor-phase deposition. The size of the hexagon varies from ~3.0 to 0.5 μm along its c-axis, and the height of the hexagons is ~10 to 15 μm. The decrease in diameter is accompanied by a series of regular facets along the microrod growth direction, resulting in numerous larger steps that significantly reduce the width of microrods. The formation mechanism of the tapered microrod involves Ga atoms having a comparatively short diffusion length, which leads them to be incorporated into a two-dimensional interface layer before attaching to the ZnO catalyst droplets, promoting microrod growth.[28, 29] Accordingly, the c-axis growth rate is slowly reduced, and tapered GZO microrods are formed. The details of the formation mechanism of the tapered microrod have been explained earlier.[27]

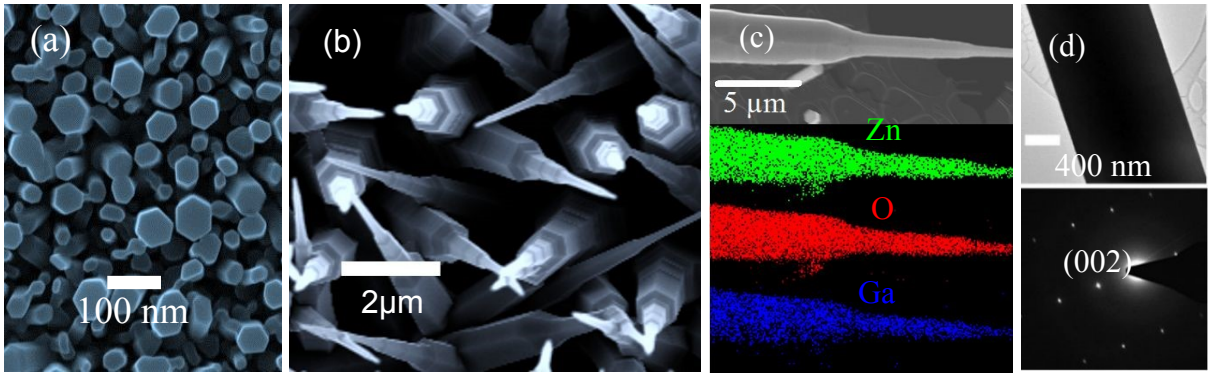

View Article Online
DOI: 10.1039/D5MA01263E

Fig. 1. Structure and morphology of ZnO and GZO microrods. (a) SEM image of an ensemble showing the characteristic hexagonal end facet. (b) SEM image showing a monolithic tapered microrod with a diameter decreasing from ~3.0 to 0.5 μm from tip to base. (c) EDS elemental maps (Zn, O, and Ga) of an isolated microrod showing uniform Ga incorporation. (d) TEM image of the lower (wider) section with indexed SAED confirming single crystalline order.

EDS elemental maps of a typical microrod reveal that the Ga is uniformly distributed along its c-axis, as depicted in Fig. 1(c). The TEM image of the base of a typical isolated tapered ZnO microrod, and the corresponding SAED pattern are displayed in Fig. 1 (d). Both the XRD (Fig. S1) and SAED patterns confirm the hexagonal wurzite structure with a strong [002] preferred orientation of the microrods. The core-level XPS spectra of the GZO microrods show Ga $2p_{3/2}$ and Ga $2p_{1/2}$ doublets (Fig. S2), which confirms the successful incorporation of Ga in ZnO microrods. Inductively coupled plasma mass spectrometry (ICP-MS, Fig. S3), with higher sensitivity at parts-per-million (ppm), quantifies the Ga concentration at 0.13 and 0.5 at% in nanorods. The 0.13 and 0.51 at.% values refer to the Ga concentrations quantified by ICP-MS for the GZO samples and are used to establish the dependence of the visible defect emission on Ga incorporation. These compositions are not intended to distinguish nanorods from microrods; rather, both nanorod ensembles and microrods were grown using corresponding Ga-containing source mixtures to compare the effect of Ga incorporation on defect emission and WGM lasing. ICP-MS was used because the Ga content is below the reliable quantitative range of EDS. EDS mapping of an isolated microrod is therefore used only to confirm the spatial presence and distribution of Ga along the microrod.

3.2 Ga-induced defect emissions in ZnO nanorods

Fig. 2 (a) depicts the room-temperature CL spectra of GZO nanorods with varying Ga doping ranging from 0 to 0.5 at%. Undoped ZnO exhibits a band-edge emission at 374 nm and a green

View Article Online
DOI: 10.1039/D5MA01263E

luminescence peaked at 506 nm. The green emission in pristine ZnO is commonly attributed to V_{Zn}.[30] With Ga incorporation, the deep-level luminescence peak shifts to a longer wavelength at 572 nm, resulting in a wavelength-tunable emission in the green to yellow. Above this doping percentage, shifting is insignificant with remarkable broadening. The Ga-induced redshift of the visible emission band has been reported earlier in GZO nanorods.[31] The band-edge emission collected at 10 K shows a dominant I_8 line at 3.359 eV, due to excitons bound to neutral Ga_{Zn} donors (Fig. S4).[32, 33]

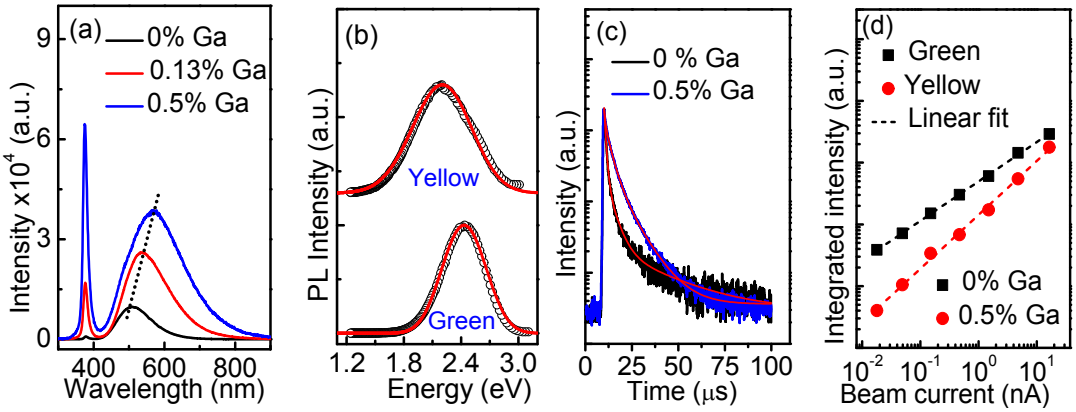

Fig. 2. Defect-enabled visible emission in GZO nanorods. (a) Room temperature CL spectra of GZO nanorods with various Ga doping. (b) Steady-state spectra of pristine and 0.5% Ga-doped ZnO nanorods were simulated using the configuration coordinate level to determine the energy position of the luminescence centers. (c) Time-resolved PL spectra of pristine and GZO nanorods showing different decay time constants of 8.2 μs for green and 5.7 μs for yellow emissions, respectively. (d) Power-resolved PL spectra of green and yellow luminescence show sublinear behaviour of recombination rate.

The energy positions of Ga-induced defects and the electron-phonon coupling strength in Ga-doped ZnO nanorods have been simulated using the configuration coordinate model, as explained in detail elsewhere.[34, 35] The simulated parameters are tabulated in Table S1. The simulated spectra agree well with the experimental spectra [Fig. 2 (b)]. The energy position of

View Article Online
DOI: 10.1039/D5MA01263E

the intraband state responsible for the green and yellow emissions can be estimated as: [36, 37] $E_A = E_g - E_{ZPL}$, where E_g is the optical bandgap, and E_A is the intraband state involved in these recombination channels. The electron-phonon coupling strength (S) is 5.9 for pristine and 7.1 for GZO nanorods. This significant increase in phonon coupling strength in Ga-doped ZnO broadens the spectral line shape.

The calculated value of the electron-phonon coupling strength is well in agreement with the reported value of ~6.5 for ZnO.[38] The acceptor state involved in the green and yellow luminesces is determined from the calculated value of E_g and E_{ZPL}. The value of acceptor energy level (E_A) for the green and yellow emission are 470 and 580 meV, respectively, above the valence band. The values of E_A for green and yellow luminescence centers agrees with the earlier reported value of 490 meV for V_{Zn}[39] and 570 meV for the Ga_{Zn}-V_{Zn} defect.[40] Ga occupying the Zn site produced Ga_{Zn} donors interacting with the V_{Zn} acceptor by coulombic attraction, forming Ga_{Zn}-V_{Zn} acceptor complexes, which involved the yellow emission and suppression of green emission.

The transient PL spectra [Fig. 2 (c)] have been measured at emission wavelengths of 506 nm (green) and 572 nm (yellow) to determine the decay time constants. The transient spectra are well fitted by a tri-exponential decay model.[41] The values of decay time and amplitude constants are displayed in Table S2. The mean decay time constants for green and yellow luminescence centers have been estimated from the following equation:[42] $\langle\tau\rangle = \sum_i A_i\tau_i^2 / \sum_i A_i\tau_i$. The green and yellow emission centers exhibit an average slow decay constant of 4.6 and 9.1 μs, respectively. The slower decay time constants for the green and yellow luminescence centers suggest that these emissions result from the recombination of an electron in the conduction band with two distinct deep states above the valence band.[41, 43] The kinetic nature of green and yellow luminescence centers is investigated by measuring the power-resolved CL

View Article Online
DOI: 10.1039/D5MA01263E

spectra. The *log-log* plot [Fig. 2 (d)] of integrated CL intensities (I) for the green and yellow emissions versus excitation power (P) follows the power law:[44, 45] $I \alpha P^k$, the values of k are 0.64 ± 0.01, and 0.82 ± 0.01, for green and yellow emission, respectively. The sublinear characteristics of green and yellow emissions indicate that these emissions are attributed to deep-level defects, which is consistent with the slower decay time constant of these emissions.

3.3 Ga-induced whispering gallery mode lasing.

The GZO nanorod ensembles are primarily used for gain and defect characterization, as their high density and weak cavity effects allow for comprehensive examination of the Ga-induced green-to-yellow emission shift, time-resolved PL, power-dependent CL, and Ga quantification. In contrast, the larger tapered GZO microrods provide the hexagonal optical cavity required for WGM lasing and spatial mode-order tuning. Fig. 3 (a) shows the room temperature WGM lasing spectra of the GZO microrod with different Ga doping concentrations. All spectra are collected from microrods of a similar diameter of 2.5 µm. Like GZO nanorods, the spectra of ZnO microrods exhibit a deep-level emission at 506 nm, accompanied by a series of optical resonance peaks. The optical resonance is due to the total internal reflection of light inside the sidewalls of the hexagonal microrod.[46] With Ga doping, the envelope spectra of ZnO microrods become broad without a significant change in the FWHM, leading to an increase in the number of resonance modes in the envelope spectrum. The peak position of the envelope spectra shifts to the higher wavelength region (572 nm), resulting in wavelength-tunable lasing in the visible spectral range of 500–600 nm. These characteristics of GZO microrods enable the realization of trap-induced tunable lasing from the green to yellow spectral region. The present study focuses on electron beam-pumped visible WGM lasing mediated by Ga-induced deep-level defect emission, rather than UV-excited near-band-edge lasing. UV optical pumping is commonly used for ZnO microlasers, but in our cavity-defect design, the lasing gain arises

View Article Online
DOI: 10.1039/D5MA01263E

from the broad visible defect band produced by Ga acceptor complexes. Electron-beam excitation is therefore particularly suitable because it provides highly localized, high-density excitation and allows spatially resolved probing along the tapered microrod, enabling direct correlation between local cavity diameter and WGM lasing order. We did not observe UV-excited lasing in the present work. UV excitation is expected to preferentially generate near-band-edge emission and to be strongly absorbed at the ZnO surface, which may limit the efficient population of the defect-mediated visible gain volume required for the present 500–600 nm WGM lasing.

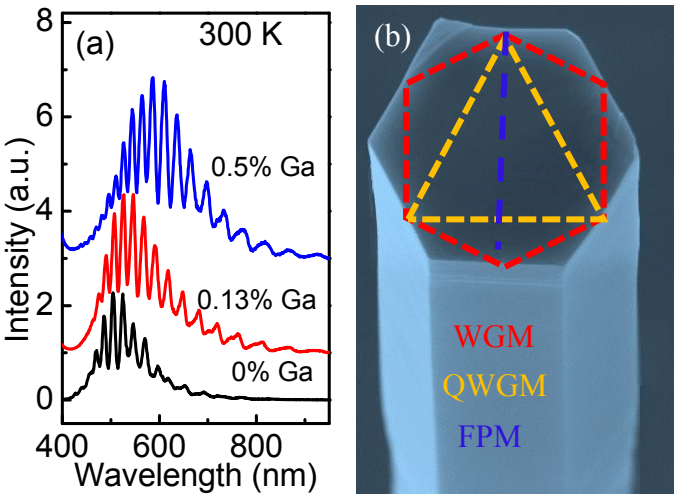

Fig. 3. Tunable visible WGM lasing enabled by Ga-induced gain redshift. (a) Room-temperature WGM lasing spectra from single GZO microrods with increasing Ga content. The emission envelope progressively redshifts with doping, enabling WGM output across ~500–600 nm. (b) Ray-optics schematics of supported cavity modes: Fabry-Perot (blue), quasi-WGM (yellow), and perimeter-circulating WGW (red).

To determine the exact resonance cavity modes, two adjacent peaks of wavelength (λ) 524.54 and 505.08 nm for pristine ZnO microrod have been considered to determine the effective path length (L) :[47]

View Article Online
DOI: 10.1039/D5MA01263E

$$\Delta\lambda = \frac{\lambda^2}{L \times (n - \lambda\frac{dn}{d\lambda})} \quad \text{.....(1)}$$

where *n* indicates refractive index and $\frac{dn}{d\lambda}$ stands for the dispersion relation. The mode spacing between the two neighboring peaks is *19.46* nm. The refractive index *n = 2.048* at *λ = 504.24* nm and the $\lambda\frac{dn}{d\lambda}$= *- 0.387* were determined from Sellmeier's relation.[48, 49]

$$n^2(\lambda) = 1 + \frac{2.4885\lambda^2}{\lambda^2 - 102.30^2} + \frac{0.2150\lambda^2}{\lambda^2 - 372.66^2} + \frac{0.2550\lambda^2}{\lambda^2 - 1850^2} \quad \text{.....(2)}$$

The effective path length using Eq. (1) is calculated for a constant value of Δ*λ,* (since Δλ is unchanged with Ga doping) and found to be *6.5 ± 0.2 μm*. The side length of the microrod is $R = 1.25\ \mu m$ determined from SEM. According to geometrical optics, three types of possible resonant cavity modes can be formed in hexagonal resonators, as shown in Fig. 3 (b): (i) Fabry-Perot (FP) modes formed between the two opposite facets of the hexagon, and the path length for this mode is $L = 2\sqrt{3}\,R$ (ii) quasi whisper gallery mode (QWGM) occurs for the light travelled among three facets of the hexagon, $L = 9\ (R/2)$ and (iii) whisper gallery mode arises for the internal reflection of light from six sides, $L = 3\sqrt{3}\,R$. The calculated path lengths are found to be *4.3, 5.6* and *6.5 μm* for FP, QWGM and WGM. The theoretically calculated effective path length is consistent with the experimental path length of WGM lasing. The resonance orders (*N*) have been determined using a classical plane-wave model of the hexagonal cavity:[50]

$$\lambda = \frac{3\sqrt{3}nR}{N + \frac{6}{\pi}\,tan^{-1}(\xi\sqrt{3n^2 - 4})} \quad \text{..... .....(3)}$$

where the factor ξ depends on the type of polarization; $\xi = n$ for transverse magnetic (TM) polarization and $\xi = \frac{1}{n}$ for transverse electric (TE) polarization. The intensity of the transverse magnetic (TM) mode is significantly weak in ZnO microrods and is not visible in the spectra. A similar-sized undoped and 0.5 at% Ga-doped microrod with a diameter of 2.5 μm was used

for these calculations. The refractive indices (n) are calculated using Sellmeier's dispersion Eq. (2) and are presented in Fig. S5. We assumed that the lower Ga doping (maximum 0.5 %) in ZnO may not significantly change the refractive index of pure ZnO. The interference orders are calculated using Eq. (3) and presented by the dotted lines in Fig. S6 (a) and S6 (b) for ZnO and GZO microrods, respectively. The uncertainty in the calculation of the WGM mode mainly arises from the uncertainty in determining the cavity diameter (±3 nm) and refractive index (±0.02). The estimated relative uncertainty (2%) in determining the *N* is smaller than the one-mode spacing, indicating the WGM mode assignment is reliable.

3.4 Geometry-dependent modulation of WGM lasing.

The size-dependent lasing characteristics were investigated using an isolated tapered microrod with a diameter varying from 0.73 nm to 2.5 µm along the c-axis, as depicted in Fig. 4 (a). Fig. 4(b) shows the WGM lasing spectra of GZO microrod under the same excitation at four different sections of a typical tapered microrod, indicated by A, B, C, and D in Fig. 4 (a). A typical isolated microrod displays 29 resonant modes at the base, with a diameter of 2.5 µm, and 3 resonant modes at the tip, with a diameter of 730 nm, as displayed in Fig. 4 (c). The decrease in lasing modes is due to the reduced overlap of WGM lasing and the gain profile of small-size cavities.[47] As the diameter decreases from around 2.5 to 0.73 µm, the WGM envelope spectral peak shifts from 585 to 552 nm, indicating a blue shift of the envelope. As the smaller cavities have a lower ability to confine light compared to the larger ones, the out-coupling efficiency increases as the cavity size decreases, leading to a blue shift of the lasing envelope peak.[51] The free spectral range (FSR) increases with decreasing the diameter of the microrod. The FSR of a cavity can be expressed as:[52] $FSR = \lambda^2/\pi D n_{eff}$, where λ denotes resonant wavelength, D is the diameter of the microrod, and n_{eff}stands for the effective refractive index of the microrod.[53] The number of resonance peaks decreases from 29 to 3 when the diameter of the microrod decreases from 2.5 to 0.73 µm due to the less overlap of the gain

View Article Online
DOI: 10.1039/D5MA01263E

profile and whispering gallery modes. The low-order (N < 3) WGMs in the visible spectrum can be achieved by modulating the defect and geometry of the microcavity.

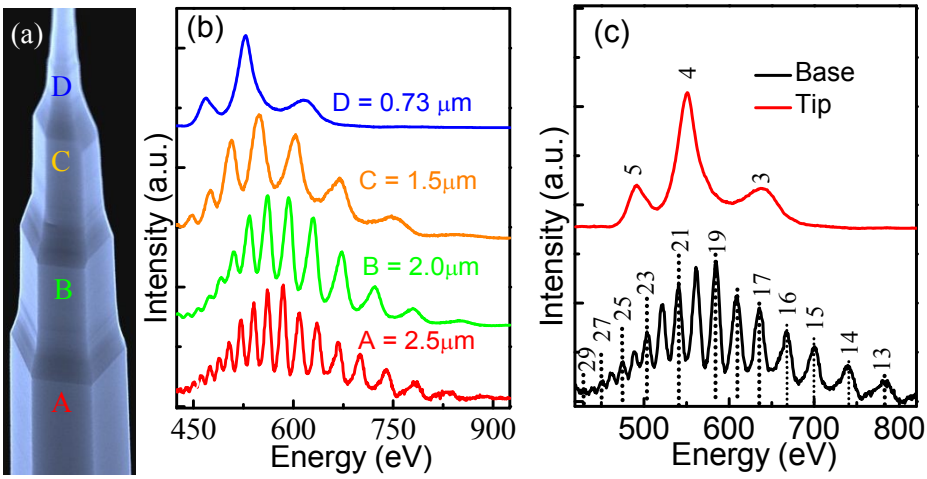

Fig. 4. Diameter-controlled WGM selection and lasing threshold. (a) SEM image of a tapered GZO microrod. The diameter increases from ~0.73 to 2.5 μm from tip to base. (b) Local optical resonance spectra acquired at successive axial positions, showing larger free-spectral range and lower mode order at smaller diameters, consistent with WGM scaling. (c) TE-polarized modes at the base showing 13-29 modes and the tip displaying 3-5 modes.

The power-dependent (0.8-3.8 μW range) spectra of the highest-intensity resonance peak, and the corresponding *log-log* plot of integrated intensity as a function of excitation power, are displayed in Fig. 5 (a) – (b). At low power, the intensity of the resonance peak exhibits sublinear behavior; however, as the power increases above a certain value (0.9 μW), known as the threshold value, the intensity of the resonance peak increases superlinearly, indicating a transition from spontaneous luminescence to stimulated emission. The position of the resonance peak shows a red shift of 14 nm, and the FWHM of the peak increases from 14 to 19 nm. The red shift of the resonance peak with increasing excitation power is due to thermal expansion and the thermo-refractive index effect, which leads to an increase in the refractive

View Article Online
DOI: 10.1039/D5MA01263E

index of the microcavity, resulting in a red shift of the resonance peak. Under the CL and lasing conditions used here, the same microrod region was continuously irradiated for 20 min, and no visible morphological damage or obvious degradation of the WGM spectral features was observed. This indicates that the tapered GZO microrods are sufficiently stable under the electron beam pumping conditions used in this study.

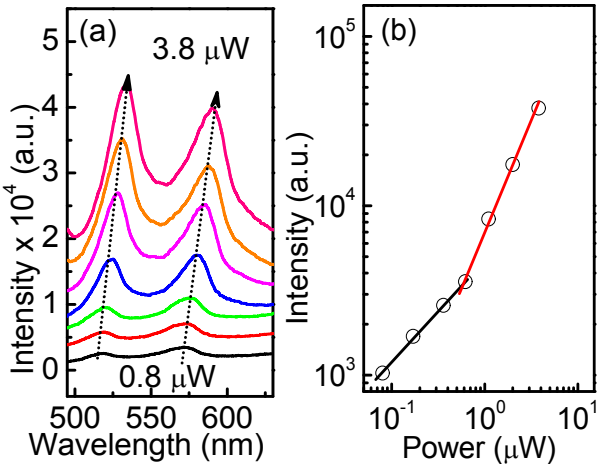

Fig. 5. Power-dependent spectra correspondence. (a) Power-dependent spectra (0.8–3.8 μW) exhibiting linewidth collapse above threshold. (b) Log-log integrated intensity versus excitation power with a clear slope change at P_{th} = 0.9 μW, marking the transition to stimulated emission.

Finite element method (FEM) simulations were carried out using COMSOL Multiphysics to model WGMs in ZnO microrods with hexagonal cross-sections. The microcavity was embedded in an air domain with scattering boundary conditions to absorb outgoing fields. The refractive index dispersion of ZnO was implemented using Sellmeier's dispersion relation and directly imported into the software.[48] A current source was set inside the 2D microcavity to excite transverse electric (TE)-polarized optical modes. A refined mesh was chosen for both the ZnO and the surrounding air to ensure convergence of the eigenmode analysis. In the simulation, the excitation source at the marked position in the 2D hexagonal microcavity (inset

View Article Online
DOI: 10.1039/D5MA01263E

of Fig. 6 (a) was kept identical across all emission wavelengths. The key parameter provided for this simulation was the position of the resonance peak. Fig. 6 (a) shows a comparison between the experimentally observed spectra and the simulated spectra for a cavity of 2.5 μm. The FEM-simulated WGM lasing spectra are well consistent with the experimentally observed lasing spectra. The analysis focused only on the position of the resonance peaks, while intensity variations were neglected.

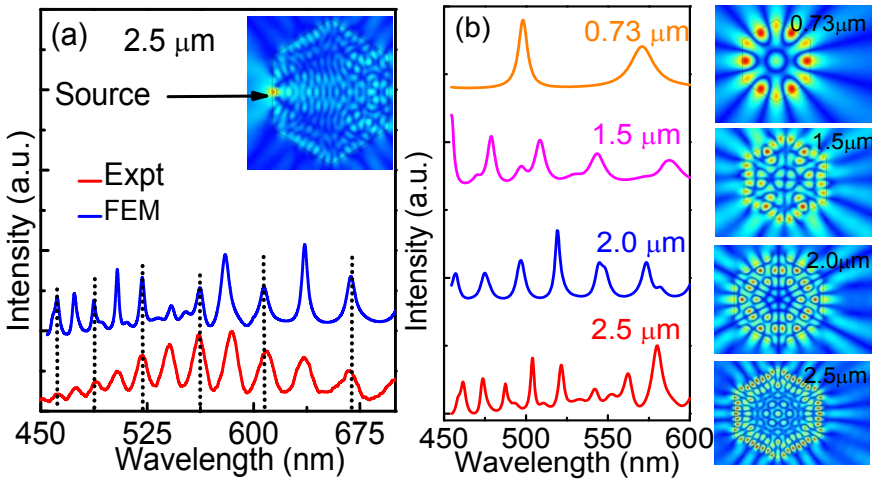

Fig. 6. Experiment–simulation correspondence and WGM scaling. (a) Measured lasing spectrum (red) overlaid with the FEM-predicted resonances (blue) for an isolated microrod of effective diameter ~2.5 μm. The inset marks the excitation site. The agreement in mode positions and free-spectral range confirms the cavity assignment. (b) FEM-computed resonance spectra for decreasing diameters (2.5→0.73 μm), showing increased free-spectral range and reduced azimuthal order as the cavity size shrinks. Right: corresponding WGM field profiles, illustrating perimeter-hugging confinement and progressive transition to low-order WGMs.

View Article Online
DOI:10.1039/D5MA01263E

To quantify how WGM order scales with cavity size, we computed resonance spectra of hexagonal ZnO microrods with diameters of 2.5, 2.0, 1.5, and 0.73 μm using finite-element eigenfrequency analysis. Fig. 6 (b) shows the simulated spectra and corresponding field maps (right panel), which identify perimeter-confined WGMs whose azimuthal order decreases with decreasing diameter. This demonstrates the strong dependence of WGM confinement and mode order on the cavity diameter. The increasing mode spacing of the microcavity with decreasing diameter agrees with the theoretical prediction of classical plane wave Eq. (3). Collectively, the agreement between the experiment and simulation in mode positions and free spectral range demonstrates that the cavity diameter serves as a reliable tuning parameter for WGM order, establishing the physical basis for spatially addressable lasing along the tapered microrod.

4 Conclusions

We demonstrated a defect–cavity co-design strategy that enables low-order visible WGM lasing in single-crystalline, hexagonal Ga-doped ZnO microrods grown by self-catalyzed vapor-phase deposition. Ga incorporation couples with native acceptors to red-shift and broaden the deep-level band, providing a controllable 500–600 nm gain window, while a growth-defined axial taper (≈ 0.73–2.5 μm) tailors the local WGM dispersion. Under electron-beam excitation, a single tapered microrod supports continuous mode-order tuning from high-order modes near the base ($N \approx 29$) to low-order modes near the tip ($N \approx 3-5$), accompanied by the expected increase in free-spectral range. Plane-wave estimates and finite-element eigenmode simulations quantitatively reproduce the measured peak positions and the evolution of mode spacing order, validating the cavity assignment.

View Article Online
DOI: 10.1039/D5MA01263E

Supporting Information

XRD GZO nanorods, XPS spectra, Time-dependent ICPMS spectra, Near band edge spectra at 10 K, simulated parameters of configuration coordinate model, Fitting parameters of decay time constants, Lasing mode number identification, Wavelength-dependent refractive indices.

Author Contribution

Rubia Anwar: Methodology, Data curation, Investigation, writing – original draft. **Cuong Ton-That**: Writing – review & editing, **M. Azizar Rahman**: Writing – review & editing, Supervision, Conceptualization.

Conflict of Interest

The authors declare that there is no conflict of interest.

Acknowledgments

The authors are grateful to CASR, Bangladesh University of Engineering and Technology (BUET) for the financial support. We are also thankful to the Department of Physics at BUET for facilitating various instruments for this study. The research work was partly undertaken on the Soft X-ray Photoelectron Spectroscopy (XPS) at the Australian Synchrotron in Australia. The authors would like to acknowledge the technical support of Herbert Yuan and James Bishop.

References

1. R. Yan, D. Gargas and P. Yang, *Nat. Photonics*, 2009, **3**, 569.
2. S. W. Eaton, A. Fu, A. B. Wong, C.-Z. Ning and P. Yang, *Nat. Rev. Mater.*, 2016, **1**, 16028.
3. Y. Sun, M. Jiang, M. Liu, K. Tang, P. Wan, B. Li, D. Shen and C. Shan, *J. Mater. Chem. C*, 2024, **12**, 7029-7040.
4. H. Dong, Y. Liu, J. Lu, Z. Chen, J. Wang and L. Zhang, *J. Mater. Chem. C*, 2013, **1**, 202-206.
5. M. C. Houghton, S. V. Kashanian, T. L. Derrien, K. Masuda and F. Vollmer, *ACS Photonics*, 2024, **11**, 892-903.
6. U. Bog, F. Brinkmann, H. Kalt, C. Koos, T. Mappes, M. Hirtz, H. Fuchs and S. Köber, *Small*, 2014, **10**, 3863-3868.
7. L. He, Ş. K. Özdemir, J. Zhu, W. Kim and L. Yang, *Nat. Nanotechnol.*, 2011, **6**, 428-432.
8. J. Shi, X. Wu, K. Wu, S. Zhang, X. Sui, W. Du, S. Yue, Y. Liang, C. Jiang and Z. Wang, *ACS Nano*, 2022, **16**, 13933-13941.
9. X. Tian, L. Wang, W. Li, Q. Lin and Q. Cao, *ACS Appl. Mater. Interfaces*, 2021, **13**, 16952-16958.

10. V. S. Ilchenko, A. A. Savchenkov, A. B. Matsko and L. Maleki, *J. Opt. Soc. Am. B*, 2003, **20**, 333-342.
11. J. Lim, A. A. Savchenkov, E. Dale, W. Liang, D. Eliyahu, V. Ilchenko, A. B. Matsko, L. Maleki and C. W. Wong, *Nat. Commun.*, 2017, **8**, 8.
12. B. Liu, A. Yamilov, Y. Ling, J. Xu and H. Cao, *Phys. Rev. Lett.*, 2003, **91**, 063903.
13. H. Cao, Y. Zhao, S. Ho, E. Seelig, Q. Wang and R. Chang, *Phys. Rev. Lett.*, 1999, **82**, 2278.
14. T.-M. Weng, T.-H. Chang, C.-P. Lu, M.-L. Lu, J.-Y. Chen, S.-H. Cheng, C.-H. Nieh and Y.-F. Chen, *ACS Photonics*, 2014, **1**, 1258-1263.
15. S. Kalusniak, H. Wünsche and F. Henneberger, *Phys. Rev. Lett.*, 2011, **106**, 013901.
16. M. A. Versteegh, D. Vanmaekelbergh and J. I. Dijkhuis, *Phys. Rev. Lett.*, 2012, **108**, 157402.
17. H. Dong, S. Sun, L. Sun, W. Zhou, L. Zhou, X. Shen, Z. Chen, J. Wang and L. Zhang, *J. Mater. Chem.*, 2012, **22**, 3069-3074.
18. H. Dong, Z. Chen, L. Sun, W. Xie, H. H. Tan, J. Lu, C. Jagadish and X. Shen, *J. Mater. Chem.*, 2010, **20**, 5510-5515.
19. K. Xu, P. Wan, M. Liu, D. Shi, C. Kan and M. Jiang, *J. Mater. Chem. C*, 2024, **12**, 17818-17828.
20. T. Nobis, E. M. Kaidashev, A. Rahm, M. Lorenz and M. Grundmann, *Phys. Rev. Lett.*, 2004, **93**, 103903.
21. G. Zhu, C. Xu, J. Zhu, C. Lv and Y. Cui, *Appl. Phys. Lett.*, 2009, **94**, 051106.
22. L. Sun, Z. Chen, Q. Ren, K. Yu, L. Bai, W. Zhou, H. Xiong, Z. Zhu and X. Shen, *Phys. Rev. Lett.*, 2008, **100**, 156403.
23. Y. Zhang, H. Zhou, S. Liu, Z. R. Tian, and M. Xiao, Nano Letters, 2009, **9**, 2109-2112.
24. C. Czekalla, C. Sturm, R. Schmidt-Grund, B. Cao, M. Lorenz and M. Grundmann, *Appl. Phys. Lett.*, 2008, **92**, 241102.
25. J. Lu, C. Xu, J. Dai, J. Li, Y. Wang, Y. Lin and P. Li, *ACS Photonics*, 2015, **2**, 73-77.
26. M. A. Rahman, M. R. Rahaman, T. Pramanik and C. Ton-That, *J. Mater. Chem.C*, 2025, **13**, 5814-5822.
27. M. A. Rahman, S. Ali, M. R. Phillips and C. Ton-That, *J. Alloys Compd.*, 2021, **895**, 162693.
28. M. Ebaid, J.-H. Kang, J. K. Lee and S.-W. Ryu, *J. Phys. D: Appl. Phys.*, 2013, **46**, 385105.
29. R. Songmuang, O. Landré and B. Daudin, *Appl. Phys. Lett.*, 2007, **91**, 251902.
30. A. Janotti and C. G. Van de Walle, *Phys. Rev. B*, 2007, **76**, 165202.
31. M. Jiang, G. He, H. Chen, Z. Zhang, L. Zheng, C. Shan, D. Shen and X. Fang, *Small*, 2017, **13**.
32. Z. Yang, D. C. Look and J. Liu, *Appl. Phys. Lett.*, 2009, **94**, 072101.
33. M. A. Rahman, M. T. Westerhausen, C. Nenstiel, S. Choi, A. Hoffmann, A. Gentle, M. R. Phillips and C. Ton-That, *Appl. Phys. Lett.*, 2017, **110**.
34. A. Alkauskas, M. D. McCluskey and C. G. Van de Walle, *J. Appl. Phys.*, 2016, **119**, 181101.
35. T. Chowdhury, R. Khatun, M. R. Rahaman and M. A. Rahman, *J. Mater. Chem. C*, 2025, **13**, 23523-23533.
36. M. Reshchikov, J. D. McNamara, F. Zhang, M. Monavarian, A. Usikov, H. Helava, Y. Makarov and H. Morkoç, *Phys. Rev. B*, 2016, **94**, 035201.
37. M. A. Rahman, M. R. Phillips and C. Ton-That, *J. Alloys Compd.*, 2017, **691**, 339-342.
38. D. Reynolds, D. C. Look and B. Jogai, *J. Appl. Phys.*, 2001, **89**, 6189-6191.
39. Z.-Q. Fang, B. Claflin, D. C. Look, Y. Dong, H. Mosbacker and L. Brillson, *J. Appl. Phys.*, 2008, **104**, 063707.
40. D. Demchenko, B. Earles, H. Liu, V. Avrutin, N. Izyumskaya, Ü. Özgür and H. Morkoç, *Physical Review B—Condensed Matter and Materials Physics*, 2011, **84**, 075201.
41. H. He, Z. Ye, S. Lin, B. Zhao, J. Huang and H. Tang, *J. Phys. Chem. C*, 2008, **112**, 14262-14265.
42. H. Huang, J. Raith, S. V. Kershaw, S. Kalytchuk, O. Tomanec, L. Jing, A. S. Susha, R. Zboril and A. L. Rogach, *Nat. Commun.*, 2017, **8**, 996.
43. W. Chebil, A. Fouzri, A. Fargi, B. Azeza, Z. Zaaboub and V. Sallet, *Mater. Res. Bull.*, 2015, **70**, 719-727.

View Article Online
DOI: 10.1039/D5MA01263E

44. M. R. Phillips, H. Telg, S. O. Kucheyev, O. Gelhausen and M. Toth, *Microsc. Microanal.*, 2003, **9**, 144-151.
45. T. Chowdhury, D. K. Paul, M. R. Rahaman, C. Ton-That and M. A. Rahman, *J. Alloys Compd.*, 2025, **1010**, 177609.
46. G. Dai, Y. Zhang, R. Liu, Q. Wan, Q. Zhang, A. Pan and B. Zou, *J. Appl. Phys.*, 2011, **110**, 033101.
47. J. Li, Y. Lin, J. Lu, C. Xu, Y. Wang, Z. Shi and J. Dai, *ACS Nano*, 2015, **9**, 6794-6800.
48. J. Liu, S. Lee, Y. Ahn, J.-Y. Park, K. H. Koh and K. H. Park, *Appl. Phys. Lett.*, 2008, **92**, 263102.
49. S. Kumar, T. Marcato, F. Krumeich, Y.-T. Li, Y.-C. Chiu and C.-J. Shih, *Nat. Commun.*, 2022, **13**, 2106.
50. S. Choi, C. Ton-That, M. R. Phillips and I. Aharonovich, *Appl. Phys. Lett.*, 2013, **103**, 171102.
51. S. K. Tang, R. Derda, Q. Quan, M. Lončar and G. M. Whitesides, *Opt. Express*, 2011, **19**, 2204-2215.
52. R. Chen, V. D. Ta and H. Sun, *ACS Photonics*, 2014, **1**, 11-16.
53. V. D. Ta, R. Chen and H. D. Sun, *Sci. Rep.*, 2013, **3**, 1362.

View Article Online
DOI: 10.1039/D5MA01263E

Data availability

The experimental and theoretical data that support the findings of this investigation are available from the corresponding author upon request.